NANO LETTERS

Letter

pubs.acs.org/NanoLett

# High-Efficiency and Air-Stable Perovskite Quantum Dots Light-Emitting Diodes with an All-Inorganic Heterostructure

Zhifeng Shi,[†] Ying Li,[†] Yuantao Zhang,[*,‡] Yongsheng Chen,[†] Xinjian Li,[*,†] Di Wu,[†] Tingting Xu,[†] Chongxin Shan,[*,†,§] and Guotong Du[‡]

[†]Department of Physics and Engineering, Zhengzhou University, Daxue Road 75, Zhengzhou 450052, China

[‡]State Key Laboratory on Integrated Optoelectronics, College of Electronic Science and Engineering, Jilin University, Qianjin Street 2699, Changchun 130012, China

[§]State Key Laboratory of Luminescence and Applications, Changchun Institute of Optics, Fine Mechanics and Physics, Chinese Academy of Sciences, Changchun 130033, China

Supporting Information

**ABSTRACT:** Perovskite light-emitting diodes (PeLEDs), because of its fundamental scientific importance and practical applications in the fields of low-cost light source or display applications, have drawn worldwide attention in recent years. However, PeLEDs available today suffer from a compromise in their emission efficiency and operation stability. In this study, we designed and fabricated a stacking all-inorganic multilayer structure by using inorganic perovskite $CsPbBr_3$ quantum dots (QDs) as the emissive layer and inorganic n-type MgZnO and p-type MgNiO as the carrier injectors, respectively. Through energy band engineering of carrier injectors by Mg incorporation and their thickness optimization, PeLEDs with maximum luminance of 3809 cd/m$^2$, luminous efficiency of 2.25 cd/A, and external quantum efficiency of 2.39% have been realized, which are much better than most PeLEDs from $CH_3NH_3PbBr_3$ films, and comparable with the highest results reported on $CsPbBr_3$ QDs LEDs. More importantly, the unencapsulated PeLEDs in a continuous current mode demonstrate a remarkable operation stability against water and oxygen degradation. After a continuous operation for 10 h under a dc bias (10.0 V), nearly 80% of the original efficiency of the PeLEDs has been retained, greatly superior to reference and other previously reported devices constructed with conventional organic carrier injectors. Our results obtained open possibilities for the design and development of high-efficiency and air-stable PeLEDs that are not dependent on expensive and less-stable organic carrier injectors.

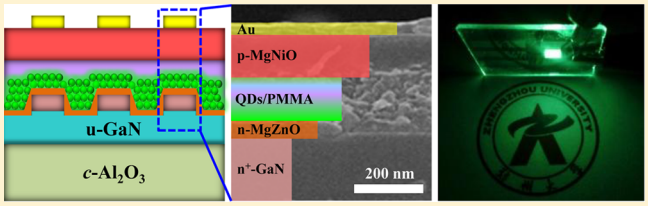


**KEYWORDS:** *Perovskite, light-emitting diodes, $CsPbBr_3$, quantum dots, operation stability*

In recent years, the newly emerging metal halide perovskite materials, in particular organometal halide perovskites ($CH_3NH_3PbX_3$, X = Cl, Br, and I), have increasingly received attention due to their great capabilities in cost-effective and large-scale manufacturing in optoelectronic devices.[1−6] This upsurge was initially driven by perovskite solar cells that attained a remarkable power conversion efficiency above 20% in the short term.[3] More recently, $CH_3NH_3PbX_3$ perovskites have been shown to possess high photoluminescence (PL) quantum efficiency, superior electrical properties, tunable emission wavelength, and high color purity that make them suitable for high-performance, low-cost, and lightweight LEDs.[4,7−9] However, operation stability has always been criticized for such materials, which are the main obstacles significantly hindering the reliable device operation and their potential application.[10] In this circumstance, inorganic cesium lead halide ($CsPbX_3$, X = Cl, Br, I) perovskite QDs, as a promising alternative approach, began to attract a great scientific attention.[11] The appealing properties of this new class of materials that might enable advances in electroluminescent devices are their outstanding optical properties owing to the quantum confinement effects and, more importantly, a higher stability than that of $CH_3NH_3PbX_3$.[12−14] It has been recognized that replacing methylammonium with inorganic cesium offers the perovskites extra thermal stability up to its melting at ∼500 °C.[15] Therefore, PeLEDs based on $CsPbX_3$ QDs have triggered a recent research interest, and typically the resulting devices often demonstrate a better electroluminescence (EL) performance than $CH_3NH_3PbX_3$ based PeLEDs.[12] Despite this, the external quantum efficiency (EQE) and operating stability of the diodes in a continuous current mode remain highly unsatisfactory and need to be improved,[14] which can be attributed to the absence of a device structure design that can not only utilize the exciton luminescent properties of the QDs, but also protect the vulnerable perovskite active layer from exposure to air ambient by n- and p-type carrier-providing layers. In previous reports, conventional carrier-injection conducting polymer or small molecules, such as poly(3,4-ethylenedioxythiophen) polystyr-

**Received:** October 1, 2016
**Revised:** December 13, 2016
**Published:** December 13, 2016

ACS Publications © 2016 American Chemical Society



DOI: 10.1021/acs.nanolett.6b04116
*Nano Lett.* 2017, 17, 313−321

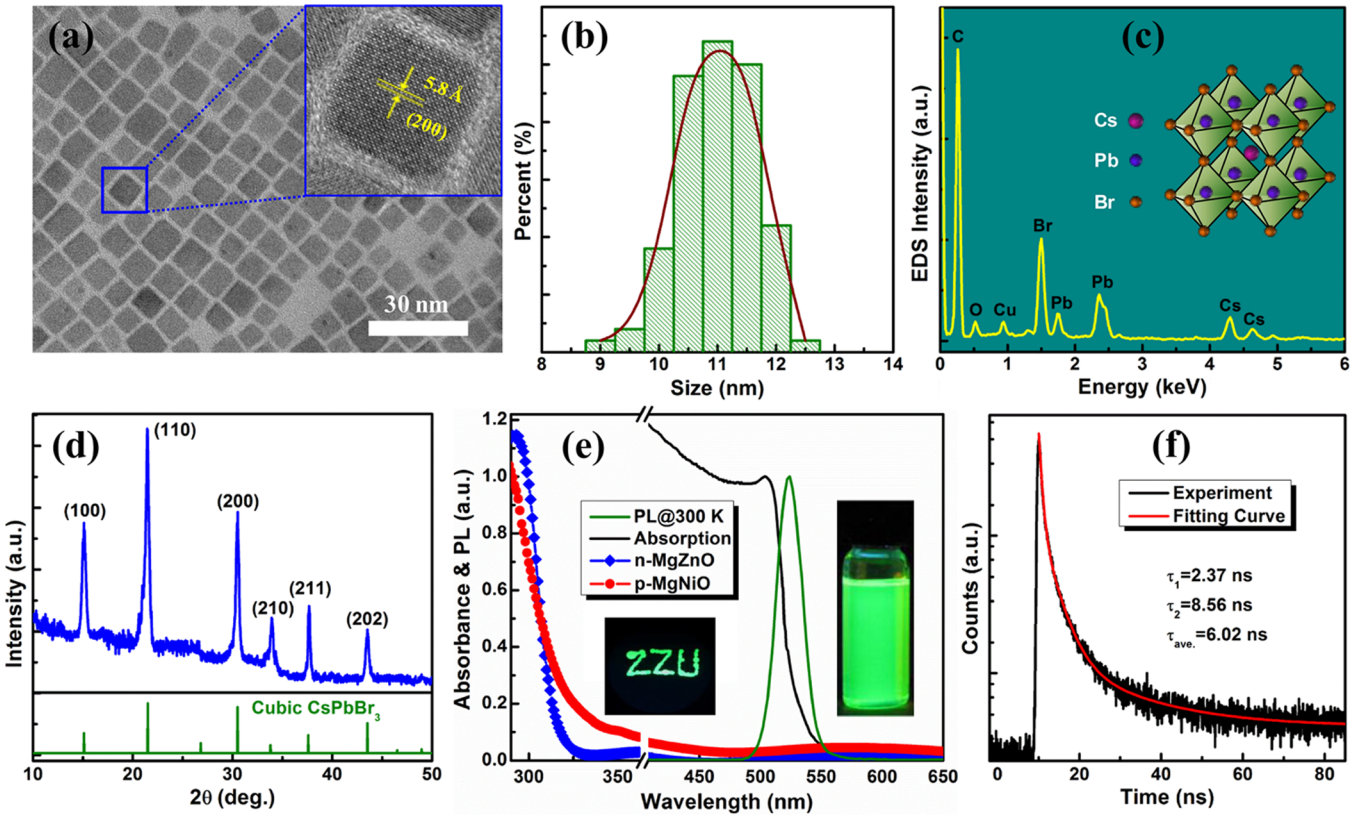


**Figure 1.** (a) TEM images of the $CsPbBr_3$ QDs. The inset shows the corresponding high-resolution TEM image, and a characteristic lattice plane distance of ~0.58 nm for cubic $CsPbBr_3$ perovskite is indicated. (b) Histogram for the size distribution of the $CsPbBr_3$ QDs. (c) EDS spectra of the obtained $CsPbBr_3$ QDs. (d) Experimental XRD spectrum (top) of a $CsPbBr_3$ QDs film and standard XRD patterns (bottom) for the cubic phases of $CsPbBr_3$. (e) Absorption spectra of the $CsPbBr_3$ QDs, n-MgZnO, and p-MgNiO films, and PL spectra of the $CsPbBr_3$ QDs measured at RT. The insets show the digital emission images of the perovskite $CsPbBr_3$ QDs and words written using the QDs solution as the ink under the excitation of a 365 nm UV lamp. (f) Time-resolved PL decay and fitting curve of the $CsPbBr_3$ QDs.

enesulfonate (PEDOT:PSS),[12,14,16−18] 2,2′,7,7′-tetrakis(*N*,*N*-*p*-dimethoxyphenylamino)-9,9′-spirobifluorene,[19,20] [6−6]-phenyl C61 butyric acid methyl ester (PCBM),[21] and 1,3,5-tris(2-*N*-phenylbenzimidazolyl) benzene,[22] have been frequently employed as the carrier injectors in PeLEDs, but their inherent chemical instability would inevitably degrade the device performance;[23] thus, a high-efficiency light emission cannot be sustained over a long running time. In this respect, the selection of suitable carrier-proving materials in PeLEDs is an important pursuit and certainly a worthwhile subject. From device emission efficiency and stability points of view, developing stable inorganic semiconductors as the carrier injectors is imperative for the continued promotion of device performance of PeLEDs on the premise of the establishment of a balanced carrier injection and confinement configuration.

In this work, we present a strategy that addresses simultaneously the emission efficiency and stability issues facing current PeLEDs' compromise. Wide bandgap metal oxide semiconductors, n-MgZnO and p-MgNiO, were employed as the electron and hole injectors to construct $CsPbBr_3$ QDs LEDs. The resulting PeLED demonstrates a relatively high luminance (3809 cd/$m^2$) and EQE (2.39%), as well as a significantly improved operation stability compared with reference and other previously reported devices constructed with conventional organic carrier injectors. It is believed that the experimental results obtained here will provide valuable information for the future design and development of high-efficiency and air-stable PeLEDs.

Figure 1a presents the typical transmission electronic microscopy (TEM) images of the solution-processed inorganic $CsPbBr_3$ QDs, which are characterized by uniformly distributed particles with a cubic shape. The diameter of the $CsPbBr_3$ QDs distributes in a narrow range of 9−13 nm with an average diameter of 11 nm (Figure 1b). The inset in Figure 1a highlights that the $CsPbBr_3$ QDs possess a well-defined crystalline structure with a characteristic lattice plane distance of ~0.58 nm, corresponding to the *d*-spacing of (200) crystal planes of cubic $CsPbBr_3$. In addition, the chemical composition of the $CsPbBr_3$ QDs was determined by applying the energy-dispersive X-ray spectroscopy (EDS) measurements. As shown in Figure 1c, no impurity element was identified except for the well-known compositions of Cs, Pb, and Br, and the incorporated Cs, Pb, and Br elements have a molar ratio of 1.00:1.05:3.21. The relatively high Br composition may be due to the reason that the Br atoms account for a large percentage on the surface compared with the corresponding bulk material.[24] The cubic structural characteristics of the produced $CsPbBr_3$ QDs were also confirmed by X-ray diffraction (XRD) pattern shown in Figure 1d. The characteristic and dominant diffraction peaks at 15.16°, 21.52°, 30.63°, 37.58°, and 43.52° can be assigned to the diffractions from (100), (110), (200), (210), (211), and (202) planes of crystalline cubic $CsPbBr_3$, consistent with the diffraction patterns of the bulk materials obtained from the JCPDS database (no. 54-0752). To analyze the optical properties of the $CsPbBr_3$ QDs, the colloidal solution was examined by ultraviolet−visible absorption and


DOI: 10.1021/acs.nanolett.6b04116
*Nano Lett.* 2017, 17, 313−321

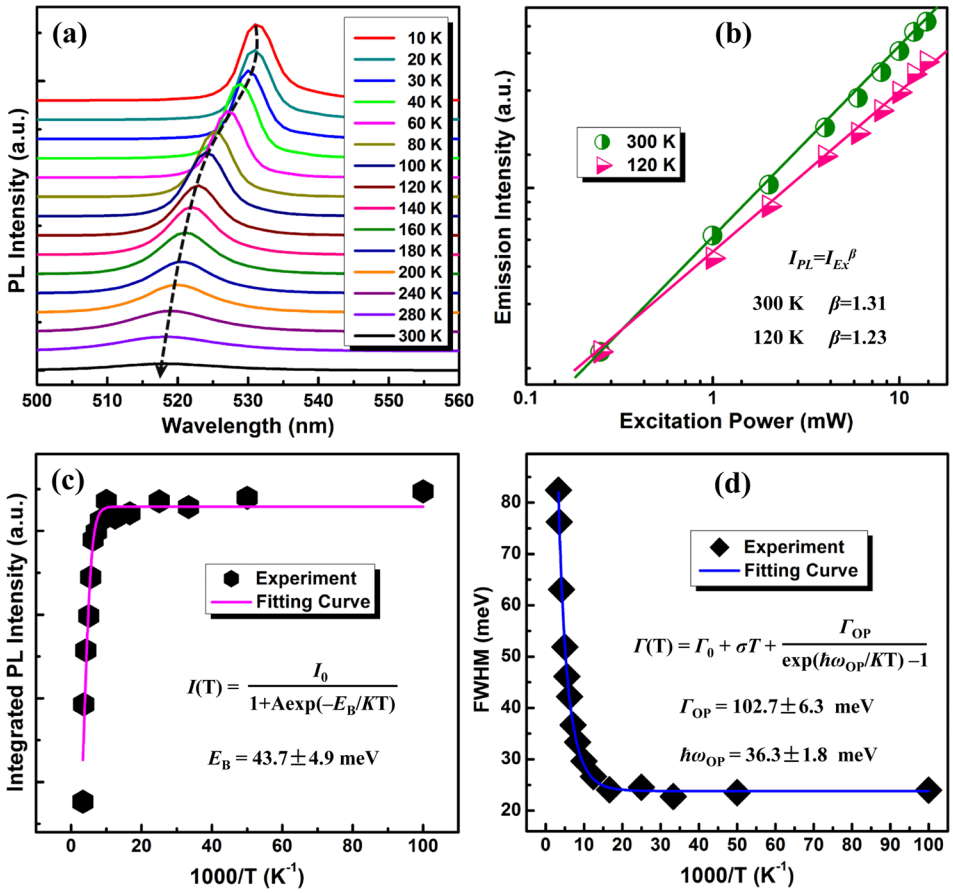


**Figure 2.** (a) Temperature-dependent PL spectra of the $CsPbBr_3$ QDs taken from 10 to 300 K. (b) The relationship between the integrated PL intensity and the excitation power of the $CsPbBr_3$ QDs at 300 and 120 K, respectively. (c) Integrated PL intensity and (d) fwhm of the $CsPbBr_3$ QDs as a function of reciprocal temperature from 10 to 300 K.

steady-state PL spectra at room-temperature (RT). As shown in Figure 1e, the absorption spectrum is dominated by a sharp peak at ~508 nm, similar to the previously reported excitonic absorption peak on solution-processed $CsPbBr_3$ QDs.[12,25] The green line shows the corresponding PL spectrum of the $CsPbBr_3$ QDs, which features a highly symmetric emission peak centered at 518 nm with a narrow line width of 17.8 nm (82 meV). Note that no sub-bandgap emission typically associated with the defects in perovskites was observed in the PL spectrum. In addition, the absorption spectra of the metal oxide semiconductors, MgZnO and MgNiO, were also provided in Figure 1e. The bandgap of $Mg_xZn_{1-x}O$ ($Mg_xNi_{1-x}O$) is approximately 3.98 eV (3.87 eV), and the corresponding value of $x$ in $Mg_xZn_{1-x}O$ ($Mg_xNi_{1-x}O$) was estimated to be 0.38 (0.23). The electrical properties of $Mg_{0.38}Zn_{0.62}O$ and $Mg_{0.23}Ni_{0.77}O$ thin films were summarized in Table S1 (Supporting Information). The absolute PL quantum yield (QY) of the $CsPbBr_3$ QDs solution was determined by using a fluorescence spectrometer with an integrated sphere with the excitation wavelength of 360 nm, and a value range of 75.6–82.2% was recorded for different batches. The PL QY of the perovskite films by spin-coating the $CsPbBr_3$ QDs solution on $SiO_2$/Si substrates was also measured, and a relatively low value of ~32.6% was obtained. In addition to being efficient in the PL QY, the as-synthesized inorganic QDs show a good stability, and only ~8.72% decay in the PL QY was observed after storage in ambient conditions for a long time of 12 days, obviously superior to the performance of organic–inorganic hybrid $CH_3NH_3PbBr_3$ QDs (Figure S1, Supporting Information). The high and stable PL QY indicates the reduction of nonradiative decay and a low defect density in inorganic $CsPbBr_3$ QDs, making the material suitable as an effective green emitter employed in PeLEDs. To gain more insight into the carrier recombination dynamics of the $CsPbBr_3$ QDs, a time-resolved PL measurement was performed (Figure 1f). The PL decay from the $CsPbBr_3$ QDs can be fitted with a biexponential decay, exhibiting a short-lived lifetime ($\tau_1$) of 2.37 ns and a long-lived lifetime ($\tau_2$) of 8.56 ns, with nearly equal contributions. Such a short radiative lifetime, along with the observed excitonic features in absorption spectrum (Figure 1e), suggest that the PL from $CsPbBr_3$ QDs originates from the excitonic recombination, unlike the recent reports for bulk perovskite films where the recombination of free electron and hole contributes to the PL and the radiative lifetimes are normally hundreds of nanoseconds.[26,27] As for the biexponential decay behavior, two different radiative mechanisms are involved. According to the research on surface-related emission in highly luminescent CdSe QDs, the short-lived PL lifetime could be ascribed to the recombination of initially generated excitons upon light absorption, and the long-lived PL lifetime may correspond to the exciton recombination with the involvement of surface states due to the stable excitons at RT.[28]

In order to better understand the optical transition mechanisms of the $CsPbBr_3$ QDs, temperature-dependent PL measurement was carried out with the temperature ranging from 300 K (RT) to 10 K. As shown in Figure 2a, with the



DOI: 10.1021/acs.nanolett.6b04116
Nano Lett. 2017, 17, 313–321

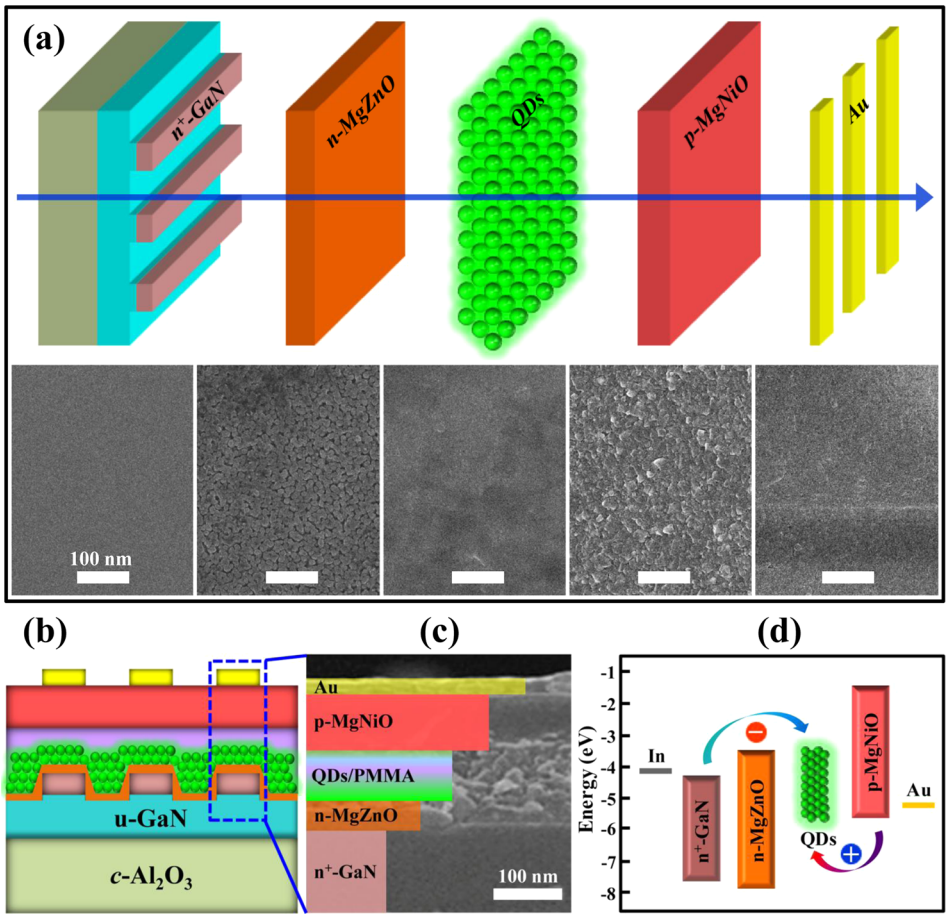


**Figure 3.** (a) Processing procedures for the fabrication of the PeLED and the corresponding top-view SEM images after each step. (b) Schematic diagram and (c) cross-sectional SEM image of the p-MgNiO/$CsPbBr_3$/n-MgZnO/$n^+$-GaN heterostructured diode. (d) Simplified energy band alignment of the multilayered heterostructure showing the conduction and valence band energy levels with respect to the vacuum level.

decrease of temperature, only one emission peak can be resolved, indicating the absence of structural phase transition in the investigated temperature region. The strong excitonic emission behavior of the $CsPbBr_3$ QDs can be verified by performing the power-dependent PL measurement. As shown in Figure 2b, a power law dependence ($I_{PL} = I_{EX}^{\beta}$, where $\beta$ denotes the nonlinear component) has been observed with $\beta$ = 1.31, confirming the excitonic characteristics of the spontaneous emission (note that $1 < \beta < 2$ accounts for the recombination of free excitons and bound excitons).[29,30] In addition, important physical parameters such as bandgap, exciton binding energy ($E_B$), and exciton−phonon interaction can be estimated based on the obtained data. Figure S2 (Supporting Information) shows the temperature sensitivity of the photon energy of the $CsPbBr_3$ QDs. We also observed a significant temperature quenching behavior of the absolute PL intensity as shown in Figure 2c. This phenomenon can be assigned to the thermally activated nonradiative recombination process, which is increasing with the temperature. The $E_B$ of the $CsPbBr_3$ QDs can be further achieved by the following equation:[31]

$$I(T) = \frac{I_0}{1 + A\exp\left(-\frac{E_B}{KT}\right)} \quad (1)$$

where $I_0$ is the emission intensity at 0 K and $A$ is a proportional constant. From the fitting, a value of 43.7 ± 4.9 meV for $E_B$ was extracted. The obtained result is much higher than the RT thermal ionization energy (~26 meV), which ensures excitons survival well above RT, highlighting the potentiality of this material in exciton-related optoelectronic devices.[32] In addition, we investigated the full-width at half-maximum (fwhm) broadening behavior of the $CsPbBr_3$ QDs to examine the exciton−phonon interaction in carrier recombination process, and the obtained data are fitted using the independent Boson model:[33]

$$\Gamma(T) = \Gamma_0 + \sigma T + \frac{\Gamma_{op}}{\exp(\hbar\omega_{op}/KT - 1)} \quad (2)$$

where $\Gamma_0$ is the inhomogeneous broadening contribution, $\sigma$ and $\Gamma_{op}$ are the exciton−acoustic phonon interaction and exciton−optical phonon contribution to the fwhm broadening, respectively, and $\hbar\omega_{op}$ is the optical phonon energy. One can see from the equation that the first term $\Gamma_0$ is the dominant contributor to $\Gamma(T)$ at low temperature levels. At relatively high temperature levels, the contributions from acoustic and optical phonon dominate over that of $\Gamma_0$, inducing a nonlinear increase of fwhm ultimately. Given the energies of $\Gamma_0$, $\Gamma_{op}$, and $\hbar\omega_{op}$ in $CsPbBr_3$ QDs being nearly independent of temperature, their constant values are found to be 36.1 ± 2.6 meV, 102.7 ± 6.3 meV, and 36.3 ± 1.8 meV, respectively. Note that the value of $\hbar\omega_{op}$ obtained matches well with the recent observation by Zhang et al. (42.2 meV),[34] and the strong exciton−phonon interaction implies the desired thermal antiquenching effect at


DOI: 10.1021/acs.nanolett.6b04116
Nano Lett. 2017, 17, 313−321

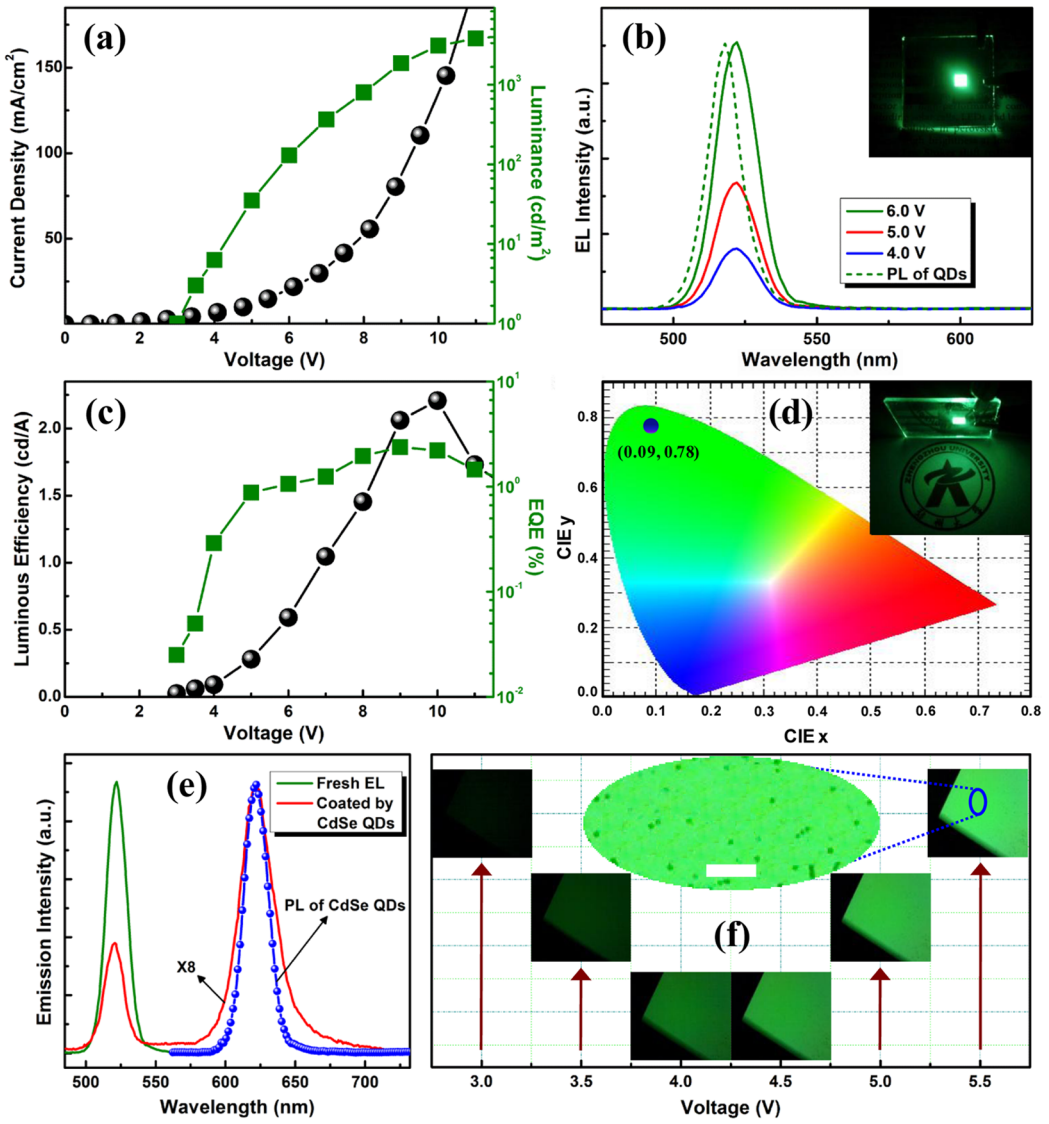


**Figure 4.** (a) Current density and luminance of the PeLED as a function of voltage under forward bias. (b) PL spectrum of the $CsPbBr_3$ QDs (dashed line), and EL spectra of the PeLED under different applied voltages, together with a typical emission photograph of the PeLED with an active area of 2 × 2 $mm^2$ (at 6.0 V). (c) Luminous efficiency and EQE versus voltage of the PeLED. (d) CIE coordinates of the PeLED under an applied voltage of 6.0 V. The inset shows a logo of Zhengzhou University illuminated by a working device. (e) Comparison of the EL spectra from the fresh and CdSe QDs-coated PeLED at the same applied voltage of 8.0 V. The blue line is the PL spectrum of the pure CdSe QDs. (f) Optical microscope images of the PeLED at different applied voltages showing the emission uniformity of a device unit. The elliptical magnified image at 5.5 V manifests a small amount of emission dark spots in a device unit. The scale bar is 100 $\mu$m.

high temperature,[35] and thus the optoelectronic devices operating with a good stability can be expected.

Figure 3a shows the main processing procedures of the studied PeLEDs fabricated from the $CsPbBr_3$ QDs employing n-MgZnO (p-MgNiO) film as the electron (hole) injector, which consist of multiple layers in the following order: patterned low-resistance $n^+$-GaN on double-polished c-$Al_2O_3$ substrates, n-MgZnO film, $CsPbBr_3$ QDs, p-MgNiO film, and Au contact electrode. The lower pane displays the corresponding top-view SEM images of the device after each processing step, and compact and uniform surface morphologies are formed. Figure 3b shows a schematic illustration of the PeLED, and the configuration of the *p*-MgNiO/$CsPbBr_3$ QDs/n-MgZnO/$n^+$-GaN heterostructure can be more clearly observed from the cross-sectional scanning electron microscope (SEM) micrograph shown in Figure 3c, from which an orderly multilayer configuration with well-defined heterointerfaces could be observed. The corresponding flat-band energy level diagram of the heterostructure was shown in Figure 3d. In the present case, the $n^+$-GaN layer is employed as the electron source layer and conducting template, as well as a transparent window. The thin MgZnO layer with an n-type conductivity can be deemed as the electron-injection and hole-blocking layer because of its matched electron affinity ($\chi$) with $CsPbBr_3$, and a relatively deep valence band energy level. Analogously, the MgNiO layer with p-type conductivity serves as the hole-injection and electron-blocking layer in virtue of its high ionization energy and low $\chi$. Thus, the carrier injection processes from the bottom n-MgZnO/$n^+$-GaN and top p-MgNiO layers to the $CsPbBr_3$ QDs can be expected, allowing the electrons and holes to recombine in the QDs active layer effectively, and further producing the light emission corresponding to the bandgap of $CsPbBr_3$ QDs.



DOI: 10.1021/acs.nanolett.6b04116
*Nano Lett.* 2017, 17, 313−321

To confirm the above inference and assess the rationality of the device structure design for efficient light emission, the fabricated device was electrically stimulated in a continuous current mode, and the corresponding EL spectra were collected from the back side of the double-polished $Al_2O_3$. Figure 4a presents the voltage-dependent variations of current density and luminance for the studied device. The turn-on voltage (which is commonly defined in literature as the voltage necessary to detect luminance of 1 cd/m$^2$) of the PeLED is about 3.0 V, much smaller than other reported perovskite QDs LEDs,[12,22,36] which presumably benefits from a reasonable device architecture with well-designed barrier-free charge injectors. Above the onset voltage, the current density and luminance rise rapidly by orders of magnitude, demonstrating a low series resistance ($R_s$), and the undesired $R_s$ or nonradiative recombination through defects does not increase in proportion with the bias voltage. A maximum luminance of 3809 cd/m$^2$ was achieved at an applied voltage of 11.0 V. Figure 4b shows the EL spectra of the device at various bias voltages, which display a single and well-defined emission peak at 522 nm with the emission intensity increasing gradually with the voltage. A slight red-shift compared with the PL spectrum taken from the QDs colloid solution may by caused by the increased carrier density and band bending of QDs at forward bias. It should be mentioned herein that no any noticeable parasitic emissions from the carrier-providing layers are observed (Figure S3, Supporting Information), which suggests that the $CsPbBr_3$ QDs serves as the primary exciton recombination zone and the recombination channels do not change during operation, and is also an indication that a balanced charge carrier transport has been achieved in the proposed device structure. In addition, the fwhm of the detected EL spectrum at 4.0 V is about 19.6 nm, and no obvious broadening behavior can be observed with the applied bias. Such a low bandwidth for color-pure devices will open up enormous opportunities for their ultrahigh-definition display applications, in which a narrow spectra width results in a better color rendering.[37] The inset of Figure 4b displays a photo taken from a device unit (2 × 2 mm$^2$) under a bias of 6.0 V. The overall emission appears green and is bright enough to be clearly observed by the naked eyes in a normal light environment. In addition, the luminous efficiency and EQE of the studied diode as a function of operated voltage were plotted in Figure 4c. Both two key parameters rise with the increasing voltage initially and then drops, which is similar to the trends observed in previous studies,[4,9,12,38] and the inevitable heating effect at high current density level might be the main cause. The peak luminous efficiencies (2.25 cd/A) and EQE (2.39%) are achieved at a current density of 110 mA/cm$^2$, much better than most PeLEDs from $CH_3NH_3PbBr_3$ films, and comparable with the best results reported on $CsPbBr_3$ QDs based LEDs (Table S2, Supporting Information). The green emission obtained corresponds to Commission International de I'Eclairage (CIE) color coordinates of (0.09, 0.78), as shown in Figure 4d, and other key device parameters are summarized in Table S3 (Supporting Information). Moreover, to assess the reproducibility of the studied diode, 15 devices were randomly selected for identical measurement in a continuous current mode. As shown by the histograms in Figure S4 (Supporting Information), an average peak EQE of 2.30% with a relative standard deviation of ∼15% can be derived, manifesting a good reproducibility of our devices.

An additional observation in our case is that the localized EL from the device unit could result in a near-field power density over 120 W/m$^2$, which presumably provides an additional freedom degree of tailoring the emission color by exciting auxiliary phosphors or other emissive semiconductor nanoparticle chromophores, thus to upgrade the display applications of the LEDs and suggest new potentials for integrated chemical and biological analysis. To explore this important possibility, we used the prepared PeLEDs to excite the CdSe QDs, which were beforehand coated onto the back side of the sapphire substrate of the device. By comparison of the EL spectra from the fresh and CdSe QDs-coated PeLED at the same bias voltage of 8.0 V (Figure 4e), one can see that the emission of CdSe QDs obtained by PeLED excitation (red solid line) shows essentially the same spectrum as that obtained by using conventional excitation source (405 nm; blue dashed line). The above results indicate that the $CsPbBr_3$ QDs PeLEDs could function as a reliable excitation source to convert the visible emission. High-performance EL emission does not mean merely large luminous efficiency and EQE, and a satisfactory emission uniformity from the device units is also important for a LED. Figure 4f shows the optical microscope images of a representative device unit taken at different applied voltages. One can observe that the green emission spreads uniformly across the entire contact area and becomes brighter on increasing the bias voltage. The elliptical magnified image at 5.5 V manifests a small amount of emission dark spots with an average size of 9.5 $\mu$m, occupying ∼2.2% of the emissive area approximately. A nonperfect metal/semiconductor contact at Au/MgNiO interface ought to bear mostly liability for the emission nonuniformity owing to the absence of postannealing process at relatively high temperatures (∼350 °C) to reduce the contact resistance as well as increase the contact adhesion. Note that no studies have reported the emission uniformity of the PeLEDs, making our results original and useful for progressing toward a practical light source.

In a recent report by You et al.,[39] perovskite solar cells with a sandwich structure ($NiO_x$/$CH_3NH_3PbI_3$/ZnO) were designed and fabricated to improve their power conversion efficiency and air stability. However, such device architecture is not applicable to PeLEDs because of their different carrier transport processes under external electric fields. Take ZnO as an example, a relatively higher $\chi$ than that of $CsPbBr_3$ goes against a barrierless electron injection process. Thus, an undesired electron injection barrier will inevitably induce a large turn-on voltage. Ternary alloy semiconductor, MgZnO, with a tunable bandgap, may be a promising replacement because the electron injection barrier with perovskite could be availably reduced. In detail, the decreased $\chi$ from −3.6 eV (ZnO) to −3.25 eV($Mg_{0.38}Zn_{0.62}O$) relative to the vacuum level will favor an almost barrier-free electron injection process. Besides, a relatively deep valence band energy level above −7.2 eV for $Mg_{0.38}Zn_{0.62}O$ implies a favorable hole-blocking effect and thereby provides an effective leakage suppression. It is the similar case for $NiO_x$ because of its shallower valence band energy level than that of $CsPbBr_3$. An additional externally forward bias is therefore needed to compensate the undesired energy barrier for hole injection. To this end, a $Mg^{2+}$ content of ∼23% (mole percent) was alloyed in the NiO film to adjust its conduction and valence bands for a matched energy level with $CsPbBr_3$. To confirm the rationality of the proposed device structure (p-$Mg_{0.23}Ni_{0.77}O$/$CsPbBr_3$ QDs/n-$Mg_{0.38}Zn_{0.62}O$/$n^+$-GaN, Device I) for an improved performance, other three PeLEDs with different structure configurations, denoted as Device II (p-$Mg_{0.23}Ni_{0.77}O$/$CsPbBr_3$ QDs/n-ZnO/$n^+$-GaN), III (p-NiO/$CsPbBr_3$ QDs/n-$Mg_{0.38}Zn_{0.62}O$/$n^+$-GaN), and IV (p-


DOI: 10.1021/acs.nanolett.6b04116
Nano Lett. 2017, 17, 313−321

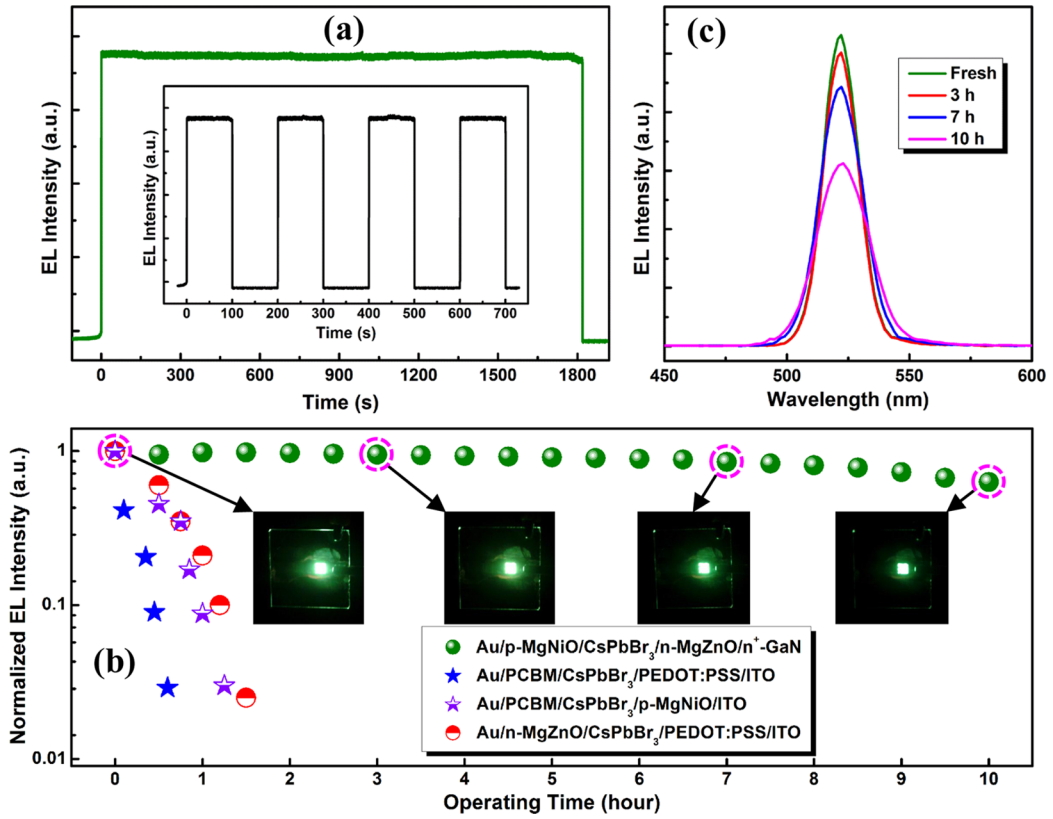


**Figure 5.** (a) Time dependence (30 min) of the RT EL intensity of the PeLED under a dc bias of 8.0 V. The inset shows the responses of the EL intensity for four switch-on/switch-off pulses at 8.0 V (100 s between each switch). (b) Emission intensity of the studied PeLED and three reference PeLEDs as a function of running time under a continuous bias of 10.0 V. The insets show the corresponding photographs of the PeLED after different running periods. (c) Evolution of the EL spectra of the studied PeLED obtained after different running periods at the same bias and measurement conditions.

NiO/$CsPbBr_3$ QDs/n-ZnO/$n^+$-GaN), were also fabricated, and their measurement results (current−voltage characteristics and EQE) were put together with those of Device I for comparison (Figure S5, Supporting Information). The above comparative studies on device performance of these four PeLEDs suggest the reasonable device structure design by using Mg incorporation into the carrier injectors to optimize the energy band alignment. Besides, the dependence of device performance on carrier injector thickness was also investigated, and the obtained results are summarized in Figure S6 (Supporting Information). One can see that the PeLEDs perform best when the $Mg_{0.38}Zn_{0.62}O$ ($Mg_{0.23}Ni_{0.77}O$) layer is about 40 nm (80 nm) in thickness by using luminous efficiency and EQE as the evaluation criterion, although the device performance shows some variation.

Kinetic experiments were further performed to characterize the stability and time response of the PeLEDs. Figure 5a illustrates the EL intensity of the diode versus running time under a dc bias of 8.0 V. One can see that the EL intensity has almost not changed over the whole running time for 30 min. Moreover, the maximum of the emission was reached very quickly in less than 30 ms after the device switch-on, and the emission was immediately cut after the device switch-off. The inset of Figure 5a shows the responses of the EL intensity for 4 switch-on/switch-off pulses at 8.0 V, and no any degradation on the device performance indicates the good stability of the studied PeLEDs.

It is generally accepted that long-term operation stability has always been a challenging issue for perovskite-based optoelectronic devices.[40] As further verification of the operation stability of the studied PeLEDs, we monitored the decay of the emission intensity of the unencapsulated device at different running periods under ambient air condition (28 °C, 30−50% humidity), in which a continuous bias of 10.0 V was applied and the emission intensity was recorded intermittently with a time interval of 0.5 h. As shown in Figure 5b, the PeLED could operate continuously for 10 h with an emission decay of ∼20%, greatly superior to reference and other previously reported devices constructed with organic electron- and/or hole-providing layers (Table S4, Supporting Information). An additional observation from Figure 5b is that a replacement of PCBM (PEDOT:PSS) with MgZnO (MgNiO), promotes the working stability of the PeLEDs to a certain extent. This observation verifies the positive roles of inorganic carrier-providing layers on the improvement in stability of PeLEDs, and the intrinsic mechanisms for such substantial improvement will be discussed later. More importantly, such a emission decay effect in the PeLEDs (p-$Mg_{0.23}Ni_{0.77}O$/$CsPbBr_3$ QDs/n-$Mg_{0.38}Zn_{0.62}O$/$n^+$-GaN) is just a transient behavior; after a relaxation time of about 5 min, the EL performance could recover to its original state. As deduced from the foregone researches, one possibility of increased heating ought to bear mostly liability in the undesired emission decay. Over the whole aging test, the temperature of the device chip will be inevitably increased, which would favor a rapid proliferation of structural defects generally. Thus, the carrier injection efficiency and radiative recombination probability will be reduced accordingly.[41] After a certain relaxation time, the temperature of the


DOI: 10.1021/acs.nanolett.6b04116
Nano Lett. 2017, 17, 313−321

device drops to RT, so both the injection current and EL performance would return to its normal level. The insets of Figure 5b illustrate the corresponding photographs of the PeLED after different running periods (0, 3, 7, and 10 h), and a slightly weakening trend on the emission intensity could be distinguished. The corresponding EL spectra, shown in Figure 5c, were also measured. One can see from the figure that the EL intensity is gradually decreased with the increase of running time, corresponding to our above discussions on emission decay.

As for the mechanisms of improved stability in the studied PeLEDs, there are many points that deserve comments herein. It is known that PCBM is a representative organic electron-providing material, which is frequently used in PeLEDs because of its matched highest (lowest) occupied molecular orbital (HOMO (LOMO)) energy levels with perovskite emissive layer.[21,42] However, the PCBM material will itself degrade through impurity adsorption because the PeLED is operated in a nonideal environment where a mass of adsorbates such as $H_2O$ and $O_2$ species exist.[43] Such contaminants incorporated in PCBM will deteriorate its electrical properties seriously, inducing an increased resistivity and the shift of HOMO and LUMO energy levels, and thus the device operation with an unsatisfactory stability can be expected. Besides, the diffusion of metal contact into the thin PCBM layer during the evaporation process is likely to increase the possibility of direct physical contact between perovskite emissive layer and metal,[39,44] which presumably induces the decomposition of perovskite and such chemical reaction process is irreversible. Analogously, the acidic and hygroscopic nature of PEDOT:PSS manifests itself an unstable carrier-providing layer for optoelectronic devices even without the exposure to the significant amount of air and moisture.[45] As a result, the emission intensity of the reference PeLED structured with Au/PCBM/$CsPbBr_3$/PEDOT:PSS/ITO drops by 95% in 0.6 h running time, as illustrated in Figure 5b. Through the replacement of PCBM with n-MgZnO (Au/n-MgZnO/$CsPbBr_3$/PEDOT:PSS/ITO), the trend of emission decay is substantially suppressed. In the initial 0.6 h, the device demonstrates a ∼ 40% decay, but after the whole aging test period (1.5 h), less than 5% of the initial performance is preserved, which is the similar case for another reference PeLED through replacement of PEDOT:PSS with p-MgNiO (Au/PCBM/$CsPbBr_3$/p-MgNiO/ITO). It is generally accepted that the inorganic metal oxides possess good stability in ambient air. Take MgZnO as an example, the sputtered MgZnO layer with a densely packed structure could not only act as a robust diffusion barrier against $H_2O$ owing to its scavenging effect[46] but also isolate the perovskite emissive layer from the metal contact. Seeking suitable substitutes for conventional PEDOT:PSS is still an arduous, but imperative task, because the researchers on perovskite-based solar cells are aware of the drawbacks from the PEDOT:PSS interlayer being unstable,[45,47] so does the situation in PeLEDs. MgNiO seems to be an attractive candidate due to its wide and tunable bandgap, well aligned with perovskites, and what's more, a superior stability against degradation by the exposure to atmosphere for a long time and inherent material stability (Table S5, Supporting Information). Moreover, the introduction of $NiO_x$ in perovskite-based solar cells to improve the device stability has already been reported and approved to be a feasible and effective solution.[39,47−50]

In conclusion, we have successfully demonstrated high-efficiency and air-stable PeLEDs by employing $CsPbBr_3$ QDs as the active layer, n-MgZnO as the electron injector, and p-MgNiO as the hole injector. The best-performing PeLED has achieved a luminance of 3809 cd/m$^2$, a luminous efficiency of 2.25 cd/A, and a EQE of 2.39%. More importantly, the unencapsulated PeLEDs demonstrate a significantly improved operation stability compared with the reference and other previously reported devices constructed with conventional organic carrier injectors. It is anticipated that our results obtained demonstrate promising inorganic carrier-providing materials than can enable high efficiency and good stability in PeLEDs, which is a considerable advance toward the realization of practical low-cost light source, facilitating the existing applications and suggesting new potentials.

## ■ ASSOCIATED CONTENT

### Supporting Information

The Supporting Information is available free of charge on the ACS Publications website at DOI: 10.1021/acs.nanolett.6b04116.

Experimental section, investigations on the PL stability of the $CsPbBr_3$ and $CH_3NH_3PbBr_3$ QDs, dependence of the photon energy on the measured temperature, indication of no parasitic emissions from the carrier-providing layers, repeat experiments of the studied PeLEDs, comparison on the device performance of four PeLEDs with different structure configurations, dependence of the device performance on the thickness of carrier injectors, Table S1 electrical properties of GaN, MgZnO, and MgNiO layers, Table S2 comparison of the device performance between our work and the reported PeLEDs, Table S3 summary on CRI, CCT, and CIE color coordinates of the studied PeLED at different applied voltages, Table S4 comparison of the operation stability between our work and the reported PeLEDs, and Table S5 investigation on the stability of p-$Mg_{0.23}Ni_{0.77}O$ thin film (PDF)

## ■ AUTHOR INFORMATION


### Corresponding Authors

*E-mail: (Y.Z.) zhangyt@jlu.edu.cn.
*E-mail: (X.L.) lixj@zzu.edu.cn.
*E-mail: (C.S.) cxshan@zzu.edu.cn.

### ORCID

Zhifeng Shi: 0000-0002-9416-3948


### Author Contributions

Z.S., Y.Z., and X.L. conceived and designed the experiments. Z.S., Y.L., and T.X. carried out the experiments. D.W. and Y.C. performed and analyzed the XRD, SEM, and PL measurements. Z.S., Y.Z., and C.S. conducted the device measurement and contributed to the data analysis. Z.S., Y.Z., and C.S. cowrote the paper, and G.D. supervised the project.

### Notes

The authors declare no competing financial interest.

## ■ ACKNOWLEDGMENTS

This work was supported by the National Natural Science Foundation of China (Nos. 11604302, 61176044, and 11504331), the China Postdoctoral Science Foundation (2015M582193), the Science and Technology Research Project of Henan Province (162300410229), the Postdoctoral Research Sponsorship in Henan Province (2015008), the Outstanding



DOI: 10.1021/acs.nanolett.6b04116
Nano Lett. 2017, 17, 313−321

Young Talent Research Fund of Zhengzhou University (1521317001), and the Startup Research Fund of Zhengzhou University (1512317003).

## REFERENCES


(1) Zhou, H. P.; Chen, Q.; Li, G.; Luo, S.; Song, T.; Duan, H. S.; Hong, Z. R.; You, J. B.; Liu, Y. S.; Yang, Y. *Science* **2014**, *345*, 542−546.

(2) Jeon, N. J.; Noh, J. H.; Kim, Y. C.; Yang, W. S.; Ryu, S.; Seok, S. I. *Nat. Mater.* **2014**, *13*, 897−903.

(3) Yang, W. S.; Noh, J. H.; Jeon, N. J.; Kim, Y. C.; Ryu, S.; Seo, J.; Seok, S. I. *Science* **2015**, *348*, 1234.

(4) Hoye, R. L. Z.; Chua, M. R.; Musselman, K. P.; Li, G. R.; Lai, M. L.; Tan, Z. K.; Greenham, N. C.; Driscoll, J. L. M.; Friend, R. H.; Credgington, D. *Adv. Mater.* **2015**, *27*, 1414−1419.

(5) Zhu, H. M.; Fu, Y. P.; Meng, F.; Wu, X.; Gong, Z.; Ding, Q.; Gustafsson, M. V.; Trinh, M. T.; Jin, S.; Zhu, X. Y. *Nat. Mater.* **2015**, *14*, 636−642.

(6) Johnston, M. B. *Nat. Photonics* **2015**, *9*, 634−636.

(7) Tan, Z. K.; Moghaddam, R. S.; Lai, M. L.; Docampo, P.; Higler, R.; Deschler, F.; Price, M.; Sadhanala, A.; Pazos, L. M.; Credgington, D.; Hanusch, F.; Bein, T.; Snaith, H. J.; Friend, R. H. *Nat. Nanotechnol.* **2014**, *9*, 687−692.

(8) Cho, H.; Jeong, S. H.; Park, M. H.; Kim, Y. H.; Wolf, C.; Lee, C. L.; Heo, J. H.; Sadhanala, A.; Myoung, N.; Yoo, S.; Im, S. H.; Friend, R. H.; Lee, T. W. *Science* **2015**, *350*, 1222−1225.

(9) Shi, Z. F.; Sun, X. G.; Wu, D.; Xu, T. T.; Zhuang, S. W.; Tian, Y. T.; Li, X. J.; Du, G. T. *Nanoscale* **2016**, *8*, 10035−10042.

(10) Yu, J. C.; Kim, D. W.; Kim, D. B.; Jung, E. D.; Park, J. H.; Lee, A. Y.; Lee, B. R.; Di Nuzzo, D.; Friend, R. H.; Song, M. H. *Adv. Mater.* **2016**, *28*, 6906−6913.

(11) Protesescu, L.; Yakunin, S.; Bodnarchuk, M. I.; Krieg, F.; Caputo, R.; Hendon, C. H.; Yang, R. X.; Walsh, A.; Kovalenko, M. V. *Nano Lett.* **2015**, *15*, 3692−3696.

(12) Song, J. Z.; Li, J. H.; Li, X. M.; Xu, L. M.; Dong, Y. H.; Zeng, H. B. *Adv. Mater.* **2015**, *27*, 7162−7167.

(13) Li, G. R.; Rivarola, F. W. R.; Davis, N. J. L. K.; Bai, S.; Jellicoe, T. C.; de la Pena, F.; Hou, S. C.; Ducati, C.; Gao, F.; Friend, R. H.; Greenham, N. C.; Tan, Z. K. *Adv. Mater.* **2016**, *28*, 3528−3534.

(14) Zhang, X.; Xu, B.; Zhang, J. B.; Gao, Y.; Zheng, Y. J.; Wang, K.; Sun, X. W. *Adv. Funct. Mater.* **2016**, *26*, 4595−4600.

(15) Stoumpos, C. C.; Malliakas, C. D.; Peters, J. A.; Liu, Z. F.; Sebastian, M.; Im, J.; Chasapis, T.; Wibowo, A. C. *Cryst. Growth Des.* **2013**, *13*, 2722−2727.

(16) Yantara, N.; Bhaumik, S.; Yan, F.; Sabba, D.; Dewi, H. A.; Mathews, N.; Boix, P. P.; Demir, H. V.; Mhaisalkar, S. *J. Phys. Chem. Lett.* **2015**, *6*, 4360−4364.

(17) Wong, B. A.; Lai, M.; Eaton, S. W.; Yu, Y.; Lin, E.; Dou, L. T.; Fu, A.; Yang, P. D. *Nano Lett.* **2015**, *15*, 5519−5524.

(18) Xing, J.; Yan, F.; Zhao, Y.; Chen, S.; Yu, H.; Zhang, Q.; Zeng, R. G.; Demir, H. V.; Sun, X. W.; Huan, A.; Xiong, Q. H. *ACS Nano* **2016**, *10*, 6623−6630.

(19) Sadhanala, A.; Kumar, A.; Pathak, S.; Rao, A.; Steiner, U.; Greenham, N. C.; Snaith, H. J.; Friend, R. F. *Adv. Electron. Mater.* **2015**, *1*, 1500008.

(20) Quintero, O. A. J.; Sanchez, R. S.; Rincon, M.; Sero, I. M. *J. Phys. Chem. Lett.* **2015**, *6*, 1883−1890.

(21) Kumawat, N. K.; Dey, A.; Kumar, A.; Gopinathan, S. P.; Narasimhan, K. L.; Kabra, D. *ACS Appl. Mater. Interfaces* **2015**, *7*, 13119−13124.

(22) Zhang, X. Y.; Lin, H.; Huang, H.; Reckmeier, C.; Zhang, Y.; Choy, W. C. H.; Rogach, A. L. *Nano Lett.* **2016**, *16*, 1415−1420.

(23) Cui, J.; Meng, F. P.; Zhang, H.; Cao, K.; Yuan, H.; Cheng, Y.; Huang, F.; Wang, M. K. *ACS Appl. Mater. Interfaces* **2014**, *6*, 22862−22870.

(24) Li, X. M.; Wu, Y.; Zhang, S. L.; Cai, B.; Gu, Y.; Song, J. Z.; Zeng, H. B. *Adv. Funct. Mater.* **2016**, *26*, 2435−2445.

(25) Yakunin, S.; Protesescu, L.; Krieg, F.; Bodnarchuk, M. I.; Nedelcu, G.; Humer, M.; De Luca, G.; Fiebig, M.; Heiss, W.; Kovalenko, M. V. *Nat. Commun.* **2015**, *6*, 8056.

(26) Priante, D.; Dursun, I.; Alias, M. S.; Shi, D.; Melnikov, V. A.; Ng, T. K.; Mohammed, O. F.; Bakr, O. M.; Ooi, B. S. *Appl. Phys. Lett.* **2015**, *106*, 081902.

(27) Dai, J.; Zheng, H. G.; Zhu, C.; Lu, J. F.; Xu, C. X. *J. Mater. Chem. C* **2016**, *4*, 4408−4413.

(28) Wang, X. Y.; Qu, L. H.; Zhang, J. Y.; Peng, X. G.; Xiao, M. *Nano Lett.* **2003**, *3*, 1103−1106.

(29) Schmidt, T.; Lischka, K.; Zulehner, W. *Phys. Rev. B: Condens. Matter Mater. Phys.* **1992**, *45*, 8989−8994.

(30) Shibata, H.; Sakai, M.; Yamada, A.; Matsubara, K.; Sakurai, K.; Tampo, H.; Ishizuka, S.; Kim, K. K.; Niki, S. *Jpn. J. Appl. Phys.* **2005**, *44*, 6113−6114.

(31) Savenije, T.; Ponseca, C. S., Jr.; Kunneman, L.; Abdellah, M.; Zheng, K. B.; Tian, Y.; Zhu, Q.; Canton, S. E.; Scheblykin, I. G.; Pullerits, T.; Yartsev, A.; Sundström, V. *J. Phys. Chem. Lett.* **2014**, *5*, 2189−2194.

(32) Sutherland, B. R.; Sargent, E. H. *Nat. Photonics* **2016**, *10*, 295−302.

(33) Rudin, S.; Reinecke, T. L.; Segall, B. *Phys. Rev. B: Condens. Matter Mater. Phys.* **1990**, *42*, 11218−11231.

(34) Zhang, F.; Zhong, H. Z.; Chen, C.; Wu, X. G.; Hu, X.; Huang, H. L.; Han, J. B.; Zou, B. S.; Dong, Y. P. *ACS Nano* **2015**, *9*, 4533−4542.

(35) Diroll, T. B.; Murray, C. B. *ACS Nano* **2014**, *8*, 6466−6474.

(36) Ling, Y. C.; Tian, Y.; Wang, X.; Wang, J. C.; Knox, J. M.; Orive, F. P.; Du, Y. J.; Tan, L.; Hanson, K.; Ma, B. W.; Gao, H. W. *Adv. Mater.* **2016**, *28*, 305−311.

(37) Huang, H.; Lin, H.; Kershaw, S. V.; Susha, A. S.; Choy, W. C. H.; Rogach, A. L. *J. Phys. Chem. Lett.* **2016**, *7*, 4398−4404.

(38) Wang, J. P.; Wang, N. N.; Jin, Y. Z.; Si, J. J.; Tan, Z. K.; Du, H.; Cheng, L.; Dai, X. L.; Bai, S.; He, H. P.; Ye, Z. Z.; Lai, M. L.; Friend, R. H.; Huang, W. *Adv. Mater.* **2015**, *27*, 2311−2316.

(39) You, J. B.; Meng, L.; Song, T. B.; Guo, T. F.; Yang, Y.; Chang, W. H.; Hong, Z.; Chen, H.; Zhou, H.; Chen, Q.; Liu, Y. S.; De Marco, N.; Yang, Y. *Nat. Nanotechnol.* **2015**, *11*, 75−81.

(40) Leijtens, T.; Eperon, G. E.; Noel, N. K.; Habisreutinger, S. N.; Petrozza, A.; Snaith, H. J. *Adv. Energy Mater.* **2015**, *5*, 1500963.

(41) Shi, Z. F.; Zhang, Y. T.; Zhang, J. X.; Wang, H.; Wu, B.; Cai, X. P.; Cui, X. J.; Dong, X.; Liang, H. W.; Zhang, B. L.; Du, G. T. *Appl. Phys. Lett.* **2013**, *103*, 021109.

(42) Hu, L.; Peng, J.; Wang, W. W.; Xia, Z.; Yuan, J.; Lu, J.; Huang, X. D.; Ma, W.; Song, H. B.; Chen, W.; Cheng, Y. B.; Tang, J. *ACS Photonics* **2014**, *1*, 547−553.

(43) Bao, Q.; Liu, X. J.; Braun, S.; Fahlman, M. *Adv. Energy Mater.* **2014**, *4*, 136−144.

(44) Dürr, A. C.; Schreiber, F.; Kelsch, M.; Carstanjen, H. D.; Dosch, H. *Adv. Mater.* **2002**, *14*, 961−963.

(45) Kwon, U.; Kim, B. G.; Nguyen, D. C.; Park, J. H.; Ha, N. Y.; Kim, S. J.; Ko, S. H.; Lee, S.; Lee, D.; Park, H. J. *Sci. Rep.* **2016**, *6*, 30759.

(46) Lee, K.; Kim, J. Y.; Park, S. H.; Kim, S. H.; Cho, S.; Heeger, A. J. *Adv. Mater.* **2007**, *19*, 2445−2449.

(47) Park, J. H.; Seo, J. W.; Park, S.; Shin, S. S.; Kim, Y. C.; Jeon, N. J.; Shin, H. W.; Ahn, T. K.; Noh, J. H.; Yoon, S. C.; Hwang, C. S.; Seok, S. I. *Adv. Mater.* **2015**, *27*, 4013−4019.

(48) Park, I. J.; Park, M. A.; Kim, D. H.; Park, G. D.; Kim, B. J.; Son, H. J.; Ko, M. J.; Lee, D. K.; Park, T.; Shin, H.; Park, N. G.; Jung, H. S.; Kim, J. Y. *J. Phys. Chem. C* **2015**, *119*, 27285−27290.

(49) Kim, J. H.; Liang, P. W.; Williams, S. T.; Cho, N.; Chueh, C. C.; Glaz, M. S.; Ginger, D. S.; Jen, A. K. *Adv. Mater.* **2015**, *27*, 695−701.

(50) Chen, W.; Wu, Y.; Yue, Y.; Liu, J.; Zhang, W.; Yang, X.; Chen, H.; Bi, E.; Ashraful, I.; Grätzel, M.; Han, L. *Science* **2015**, *350*, 944−948.




DOI: 10.1021/acs.nanolett.6b04116
*Nano Lett.* 2017, 17, 313−321